Journal of Biomedical Optics

SPIEDigitalLibrary.org/jbo

Application of multiple artificial neural networks for the determination of the optical properties of turbid media

Marion Jäger
Florian Foschum
Alwin Kienle

SPIE

Application of multiple artificial neural networks for the determination of the optical properties of turbid media

Marion Jäger, Florian Foschum, and Alwin Kienle
Institut für Lasertechnologien in der Medizin und Meßtechnik an der Universität Ulm, Helmholtzstraße 12, 89081 Ulm, Germany

Abstract. We determined the optical properties of turbid media from simulated spatially resolved reflectance (SRR) curves using an artificial neural network (ANN). In order to improve the performance of our method, multiple ANNs were applied for this problem. First, Monte Carlo (MC) simulations were performed using random optical properties which are relevant for biological tissue. For a better performance of the ANN in respect of SRR measurements, the exact setup geometry was taken into account for the MC simulations. Second, the performed simulations were classified into different categories according to their shape. Third, multiple ANNs which were adjusted to these categories, were used to solve the inverse problem, i.e., the determination of the optical properties from SRR curves. Finally, these ANNs were applied to determine the optical properties of simulated SRR curves out of the range 0.5 $mm^{-1} < \mu_s' < 5$ mm^{-1} and 0.0001 $mm^{-1} < \mu_a < 1$ mm^{-1}. The average relative error was 2.9% and 6.1% for the reduced scattering coefficient μ_s' and for the absorption coefficient μ_a, respectively. © *2013 Society of Photo-Optical Instrumentation Engineers (SPIE)* [DOI: 10.1117/1.JBO.18.5.057005]

Keywords: multiple artificial neural networks; Monte Carlo simulation; diffusion theory; spatially resolved reflectance; optical properties; turbid media.

Paper 130060R received Feb. 1, 2013; revised manuscript received Apr. 5, 2013; accepted for publication Apr. 15, 2013; published online May 15, 2013.

1 Introduction

The noninvasive determination of the optical properties of tissue is an important research area.[1–7] To the authors' knowledge, Farrell et al.[8] reported, for the first time, the determination of the optical properties of simulated experimental data applying an artificial neural network (ANN) that was trained using the diffusion theory (DT). In addition, phantom and *in vivo* evaluation studies were performed by Farrell et al.[9] Subsequently, due to the shortcomings of DT, Kienle et al.[10] used an ANN that was trained with Monte Carlo (MC) simulations for the determination of the optical properties from reflectance measurements. Root mean square (RMS) errors of 2.6% for μ_s' and 14% for μ_a from absolute measurements of tissue-simulating phantoms were received. The ANN was trained with optical properties out of the range 0.002 to 0.1 mm^{-1} for μ_a and 0.5 to 2.0 mm^{-1} for μ_s'. Warncke et al.[11] also used MC simulations for the training of the ANN. They determined the optical properties out of the range 0.02 to 1 mm^{-1} for μ_a and 0.6 to 2.5 mm^{-1} for μ_s' with an RMS error of 28% for μ_a and 9% for μ_s' for simulated spatially resolved reflectance (SRR) curves. Zhang et al.[12] used MC simulations, as well as measurements of tissue-simulating phantoms, to train an ANN. They reported that the ANN trained with MC simulations cannot properly estimate the optical properties of measurement data collected with their measurement setup. Thus, an ANN trained with measurement data was used to determine the optical properties. An ANN approach for the determination of the optical properties of two-layered media was presented by Wang et al.[13] using a fibre-optic based reflectance system. Wang et al.[13] used MATLAB for the training of the ANN with reflectance data from MC simulations. Additionally, they showed an experimental evaluation of SRR measurement of layered tissue optical properties in the UV-Vis at three wavelengths. Later, Wang et al.[14] showed an ANN model that determined the optical properties in two stages. If the absorption coefficient calculated by the first ANN was below a certain value, a second ANN was applied for the determination of the optical properties. Yaqin et al.[15] presented another approach which included an ANN in combination with a preprocessing technique, the principal component analysis, for the determination of the optical properties. Their method simplifies the ANN structure and reduces the time for training the ANN. Their optical property range for μ_s' was between 0.1 mm^{-1} and 2.0 mm^{-1} and for μ_a between 0.01 mm^{-1} and 0.1 mm^{-1} and RMS errors of 4.6% for μ_s' and 9.2% for μ_a were received.

In a previous publication, we showed the noninvasive determination of the brain absorption in a five-layered model of the human head.[16] Furthermore, an ANN was used for the determination of the optical properties of scalp and skull in a four-layered model of the human head as well as for the determination of the optical properties of two-layered media.[17] In this study, for the first time, multiple ANNs were applied for the solution of the inverse problem of simulated SRR curves. We show that multiple ANNs improve the results significantly. We used MC simulations, considering the setup geometry, for the training of the ANN. Therefore, our ANN can be applied for the precise determination of the optical properties of measurement data.

2 Forward Problem

The forward problem, which is the calculation of theoretical SRR curves from the given optical properties, can be solved using different methods. For a semi-infinite medium, the DT

Address all correspondence to: Marion Jäger, Institut für Lasertechnologien in der Medizin und Meßtechnik an der Universität Ulm, Helmholtzstraße 12, 89081 Ulm, Germany. Tel: +49 (0)731 1429-118; Fax: +49 (0)731 14 29-442; E-mail: marion.jaeger@ilm.uni-ulm.de

0091-3286/2013/$25.00 © 2013 SPIE

is, in some cases, a good approximation of the radiative transfer equation (RTE). The analytical solution is e.g., described by Kienle and Patterson.[18] We note that, recently, exact analytical solutions of the RTE were derived for a semi-infinite medium.[19] An exact solution of the RTE can also be achieved using a numerical solution, for example, a MC simulation.[20] However, an infinitely large number of photons is needed for an exact solution of a MC simulation without noise. In addition, MC simulations allow the consideration of an arbitrary setup geometry for a better description of SRR measurements.[21] We used our self-written MC simulations considering the measurement geometry as explained below.

2.1 *Principles of the MC Simulation*

The principles of the used MC simulations are similar as those described by Wang et al.[20] For liquid phantoms consisting of buffer, Intralipid and ink, we assumed a refractive index of $n = 1.33$. Furthermore, for a more exact description of our sample, we measured the phase function for Intralipid using a homebuild goniometer (not shown). A similar phase function, as published by Michels et al.,[22] was obtained and applied in the MC simulation.

In order to achieve optimal results, we adjusted our MC simulations that they reflect our measurement setup. Performing measurements, the SRR of a semi-infinite medium was measured using a charge-coupled device (CCD)-camera as described by Foschum et al.[21] The light from a xenon lamp was coupled into an optical fibre and the sample was illuminated with an angle of 11 deg relative to the surface normal. Thereby, the sample-sided end of the optical fibre was imaged on the surface of the semi-infinite medium. A 400 μm top hat was obtained at the surface of the sample. As described by Kienle and Foschum,[23] the angular distribution of the emitted photons from the semi-infinite medium do not have a cosine dependence. Using a variance reductions method, the probability of the photon to hit the CCD-chip is calculated and all the photons that pass through the aperture are collected.[24] That means that the reflected light from one position on the sample only reaches the CCD-chip when it is radiated in a certain solid angle. Foschum et al.[21] used this measurement setup and transferred those characteristics into the MC simulations.

2.2 *MC Simulation for the Training of the ANN*

MC simulations were used for the training, validating, and testing of the ANN (see Sec. 3). The optical properties, covering those usually found in biological tissue, were randomly chosen out of the range $0.0001\ \text{mm}^{-1} < \mu_a < 1\ \text{mm}^{-1}$ for the absorption coefficient and out of the range $0.5\ \text{mm}^{-1} < \mu_s' < 5\ \text{mm}^{-1}$ for the reduced scattering coefficient and SRR curves were simulated.

Three data sets, each consisting of 2,000 theoretical SRR curves, were simulated. The first data set was used for the training of the ANN, the second for the validation, and the third for the testing of the ANN (see Sec. 3.1). In case of the validation and testing datasets, the optical properties for the reduced scattering coefficient

$$\mu_s' = 0.5 + \xi \cdot (5 - 0.5)\ \text{mm}^{-1} \tag{1}$$

and for the absorption coefficient

$$\mu_a = 10^{-\{\xi[-\log_{10}(0.0001)+\log_{10}(1)]-\log_{10}(1)\}}\ \text{mm}^{-1}, \tag{2}$$

are randomly chosen out of the given range with ξ being a random number between 0 and 1. For the training data set, the range was 5% larger. We used 10^6 photons for $\mu_a < 0.1\ \text{mm}^{-1}$ and $7 \cdot 10^6$ photons for $\mu_a > 0.1\ \text{mm}^{-1}$ in the MC simulations. Therewith, the noise range in the MC simulations is equivalent to the experimental data.

3 Inverse Problem

The opposite approach to the forward problem is the inverse problem. That is, the determination of the optical properties from SRR curves. These reflectance curves can be obtained from
measurements as well as from simulations of the SRR. There are multiple methods to calculate the optical properties for a given SRR curve. One method is a nonlinear regression and another method is the application of an ANN as explained below.

3.1 *ANN*

The theoretical principles of the used ANN are explained by Boone et al.[25] We applied an ANN consisting of an input layer, a hidden layer, and an output layer. Each layer has multiple neurons. The 11 neurons of the input layer contain certain information of the SRR curve and the 11 neurons of the hidden layer are located between the input and the output layer. The 2 neurons of the output layer represent by means of the ANN calculated absorption coefficient $\mu_a^{\text{ANN},i}$ and reduced scattering coefficient $\mu_s'^{\text{ANN},i}$ of the i'th SRR curve. Weights that connect the neurons of the input layer with the neurons of the hidden layer and the neurons of the hidden layer with the neurons of the output layer define the strength of the connections.

In the first step, the ANN is trained with a training dataset consisting of N SRR curves. At the beginning of the training process, the weights are randomly chosen out of the range -0.3 and $+0.3$ as described by Boone et al.[25] Using the gradient descent method, the weights are modified iteratively in order to adjust the optical properties, in other words, the result in the output layer. This result is compared with the true optical properties known from the MC simulations in order to verify the performance of the ANN. Therefore, the relative RMS error

$$\sigma_{\text{rel}} = \sqrt{\frac{1}{2 \cdot N}\sum_{i=1}^{N}\left[\left(\frac{\mu_a^{\text{ANN},i} - \mu_a^{\text{MC},i}}{\mu_a^{\text{MC},i}}\right)^2 + \left(\frac{\mu_s'^{\text{ANN},i} - \mu_s'^{\text{MC},i}}{\mu_s'^{\text{MC},i}}\right)^2\right]} \tag{3}$$

between by means of the ANN calculated optical properties and the true optical properties known from the MC simulations is minimized.

After the training process, the optimal weights for the training dataset are determined. During the following executing phase, these weights can be used to calculate the optical properties of an unknown SRR curve. In order to avoid overfitting, we used a second dataset consisting of N SRR curves (called validation dataset) during the training process. Still, the ANN is trained with the above mentioned training dataset and the weights that yield a minimal error σ_{rel} for the training dataset are used during the training process. Additionally, the weights

that give a minimal error σ_{rel} for the validation dataset are stored after every iteration. These weights are used to solve the inverse problem in the executing phase of the ANN.

Since the MC simulations already consider the used setup geometry, our trained ANN is suitable for the determination of the optical properties of measured SRR curves. Only relative SRR curves can be measured with the measurement setup explained by Foschum et al.[21] That is why we have to process all reflectance curves (measured as well as simulated SRR curves) to relative curves. It is important to treat all curves the same way in order to obtain suitable input data for the ANN. Relative curves were obtained using the below explained normalization of the logarithm of the SRR curve. To achieve this the function

$$\log[R(\rho)_{\mathrm{fit}}] = a + b \cdot \rho + c \cdot \rho^2 + d \cdot \sqrt{\rho}, \qquad (4)$$

that was found empirically, is fitted to every logarithmic SRR curve in order to smooth the noise. The fitted, logarithmic reflectance is $\log[R(\rho)_{\mathrm{fit}}]$, the radial distance is denoted with ρ and a, b, c, d specify the coefficients of the function. The area A under the curve, between the reflectance value at $\rho = 1$ mm and the reflectance value at the position where the reflectance decreased by 2.2 orders of magnitude in relation to the reflectance value at $\rho = 1$ mm, was calculated using Eq. (4). Additionally, the radial distance $\bar{\rho}$ where the reflectance decreased by 2.2 orders of magnitude relative to the reflectance value at $\rho = 1$ mm was stored. Thereafter, the average height of the curve $h = A/(\bar{\rho} - 1)$ was calculated and shifted to 0 of the y-axis in order to achieve relative SRR curves. We note that achieving relative SRR curves by dividing every curve through a certain reflectance value is problematic because one reflectance value can contain some errors as noise or systematic errors. For the analysis of the SRR curves, we have to take into account the limitation given by our measurement setup. It is only possible to measure the SRR up to the radial distance $\rho = 23$ mm and over a range of 3 orders of magnitude relative to the reflectance value at about $\rho = 1$ mm. The smallest radial distance is $\rho = 1$ mm because of the errors caused by the illumination profile that is not an exact top hat.

In the following, we first explain the performance of one ANN (see Sec. 3.2) and, thereafter, the performance of multiple ANNs (see Sec. 3.3).

3.2 *One ANN*

First, one ANN was used to solve the inverse problem. After we have achieved relative SRR curves, the above mentioned function [see Eq. (4)] was again fitted to the resulting logarithmic SRR curves. Some results can be seen in Fig. 1. The minimum and maximum reflectance value, of every curve, was determined under consideration of the limitation given by our measurement setup. After that, the minimum of all maximum values and the maximum of all minimum values (depicted in Fig. 1) was calculated in order to define the possible range of all SRR curves. (Using the reflectance values at fixed radial distances as input values would limit the applicable radial distances between 1 mm and 3 mm due to the strong decrease of reflectance curves with high absorption coefficients and the maximal 3 orders of magnitude relative to the reflectance value at $\rho = 1$ mm that can be measured with our measurement setup). For that reason, 11 reflectance values $R(j)$ $(j = 1 \ldots 11)$, with an equidistant decrease in the logarithm of the reflectance, have been chosen out of the measurable range as depicted in Fig. 2. The

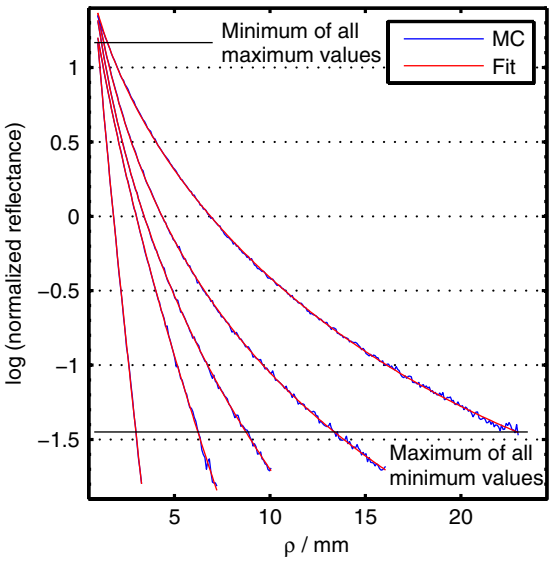

Fig. 1 Some relative SRR curves from the MC simulations and the corresponding fitted SRR curve.

corresponding radial distance values $\rho[R(j)]$ serve as input values for the ANN (see Fig. 2). The input values, as well as the output values, of each neuron were scaled in the range 0.1 to 0.9. This range was found empirically. It follows for the scaled radial distance value of neuron $n(j)$

$$\rho^{\mathrm{sc}}_{n(j)} = \frac{\rho[R(j)] - \rho^{\min}_{n(j)}}{\rho^{\max}_{n(j)} - \rho^{\min}_{n(j)}} \cdot (0.9 - 0.1) + 0.1, \qquad (5)$$

with $\rho^{\min}_{n(j)}$ being the smallest radial distance of neuron $n(j)$ of all N reflectance curves of the training dataset and $\rho^{\max}_{n(j)}$ being the largest radial distance.

Equally, the scaling for the reduced scattering coefficient and the absorption coefficient was performed. It follows for the scaled reduced scattering coefficient

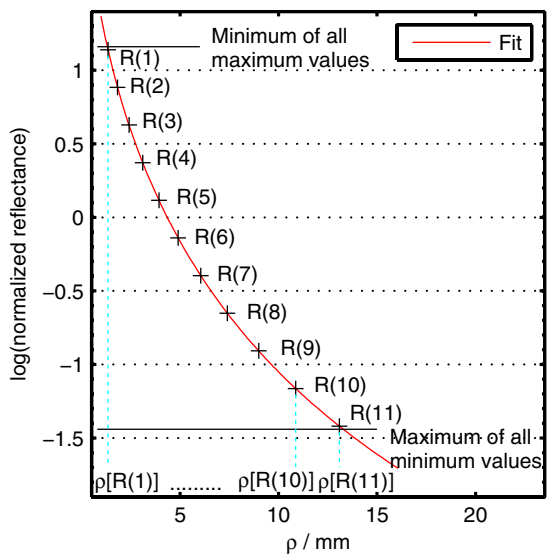

Fig. 2 One relative SRR curve from Fig. 1 and the chosen 11 reflectance values $R(j)$ as well as the corresponding radial distance values $\rho[R(j)]$.

$$\mu_s'^{\mathrm{sc}} = \frac{\mu_s' - \mu_s'^{\min}}{\mu_s'^{\max} - \mu_s'^{\min}} \cdot (0.9 - 0.1) + 0.1 \qquad (6)$$

and for the scaled absorption coefficient

$$\widetilde{\mu_a^{sc}} = \frac{\log_{10}(\mu_a) - \log_{10}(\mu_a^{\min})}{\log_{10}(\mu_a^{\max}) - \log_{10}(\mu_a^{\min})} \cdot (0.9 - 0.1) + 0.1, \qquad (7)$$

with $\mu_s'^{\min}$ being the smallest reduced scattering coefficient μ_s' found in the N SRR curves of the training dataset, and $\mu_s'^{\max}$ being the largest reduced scattering coefficient. Much better results are achieved if we use the logarithm of the absorption coefficient as output value for the performance of the ANN. The smallest absorption coefficient μ_a, in the N SRR curves of the training dataset, is described by $\mu_a^{\min}$ and $\mu_a^{\max}$ is the largest absorption coefficient.

The ANN was trained with 100 SRR curves from the training dataset and validated with another 100 SRR curves from the validation dataset. The weights that have a minimal relative RMS error σ_{rel} for the validation dataset were stored. Using those weights, the error of an unknown testing dataset was calculated. In Sec. 4, the average relative error, for this testing dataset, is shown. We remark that we used 100 SRR curves for the training since, with this amount of SRR curves, good results were achieved. Using 200, 500 and 2,000 SRR curves, for the training of the ANN, do not improve the results but need more computation time. We found that too many SRR curves used for the training even lead to larger errors since the ANN is not able to adjust the weights for all curves. For the testing, we used 2,000 curves in order to have good statistics and to directly compare the results to multiple ANNs (see Sec. 4).

Table 1 Summary of the categorization into 23 ANNs using presorting, the last measurable radial distance value ρ_{last}, the first and second derivative of the fitted function $\log[R(\rho)_{\mathrm{fit}}]$. Additionally, the smallest and largest optical properties for the particular ANNs are shown.

ANN no.	presorting	ρ_{last} [mm]	R''	R'	$\mu_s'^{\min}$ [mm^{-1}]	$\mu_s'^{\max}$[mm^{-1}]	$\mu_a^{\min}$[mm^{-1}]	$\mu_a^{\max}$[mm^{-1}]
1	I	—	—	—	0.5	1.1	$9.600e^{-5}$	$1.155e^{-2}$
2	II	A	a	1	0.5	2.3	$6.644e^{-2}$	$9.743e^{-1}$
3	II	A	a	2	0.5	2.2	$2.266e^{-2}$	$3.127e^{-1}$
4	II	A	a	3	0.5	2.1	$8.496e^{-3}$	$1.495e^{-1}$
5	II	A	a	4	0.5	2.1	$2.425e^{-3}$	$6.562e^{-2}$
6	II	A	a	5	0.5	2.0	$2.404e^{-4}$	$2.405e^{-2}$
7	II	A	a	6	0.5	2.0	$9.563e^{-5}$	$1.814e^{-2}$
8	II	A	b	1	1.8	3.9	$2.928e^{-2}$	$3.757e^{-1}$
9	II	A	b	2	2.1	3.8	$9.088e^{-3}$	$7.178e^{-2}$
10	II	A	b	3	2.0	3.7	$2.936e^{-3}$	$2.018e^{-2}$
11	II	A	b	4	2.0	3.5	$5.725e^{-4}$	$7.370e^{-3}$
12	II	A	b	5	2.0	3.5	$9.768e^{-5}$	$2.777e^{-3}$
13	II	A	b	6	1.9	3.5	$9.533e^{-5}$	$1.208e^{-3}$
14	II	A	c	1	3.4	5.2	$2.530e^{-2}$	$1.759e^{-1}$
15	II	A	c	2	3.5	5.2	$7.944e^{-3}$	$4.704e^{-2}$
16	II	A	c	3	3.4	5.2	$3.118e^{-3}$	$1.439e^{-2}$
17	II	A	c	4	3.4	5.2	$1.093e^{-3}$	$6.593e^{-3}$
18	II	A	c	5	3.4	5.2	$3.008e^{-4}$	$3.006e^{-3}$
19	II	A	c	6	3.4	5.2	$1.004e^{-4}$	$1.076e^{-3}$
20	II	A	c	7	3.2	5.2	$9.628e^{-5}$	$5.744e^{-4}$
21	II	B	—	1	1.7	5.2	$3.367e^{-1}$	1.047
22	II	B	—	2	1.0	5.2	$2.059e^{-1}$	1.016
23	II	B	—	3	0.7	5.2	$1.046e^{-1}$	1.016

3.3 *Multiple ANNs*

In order to achieve better results, multiple ANNs were applied to solve the inverse problem. Using 6,000 SRR curves, 23 ANNs were trained, validated, and tested. First of all, the SRR curves have to be classified according to their shape. These classifications divide the SRR curves in different groups, in other words the different ANNs. This restricts the limits of the optical property range to certain ranges. It can be seen, in Table 1, that each ANN was responsible for a certain range of the absorption coefficient and the reduced scattering coefficient, respectively. We remark that some overlapping of the ANNs was considered. Apart from that classification, the approach of multiple ANNs (in other words the calculation of the input values, output values etc.) is analogue to the approach of one ANN.

3.3.1 *Classification of the curves*

Since we have a quite large range for the absorption coefficient ($0.0001\ \mathrm{mm}^{-1} < \mu_a < 1\ \mathrm{mm}^{-1}$) and for the reduced scattering coefficient ($0.5\ \mathrm{mm}^{-1} < \mu_s' < 5\ \mathrm{mm}^{-1}$), it it useful to group the SRR curves, according to their shape, into different categories in order to obtain a better performance of the ANNs. We found relationships between the shape of the curve and the optical properties that made it possible to divide the optical property range in many smaller categories. For each category, a special adjusted ANN was applied. The classification of the SRR curves is shown below.

3.3.2 *Presorting of the curves*

Before the categorization of the curves was performed, 2,000 SRR curves of the training dataset were presorted in group I and II. As stated in Sec. 3.1, with the CCD-camera, it is possible to measure the SRR up to the radial distance $\rho = 23$ mm and over a range of 3 orders of magnitude relative to the reflectance value at the radial distance of about $\rho = 1$ mm. Some SRR curves, with lower absorption and reduced scattering coefficients, already reach at the maximal measurable radial distance of $\rho = 23$ mm a decrease between 2.2 and 3 orders of magnitude relative to the reflectance value at $\rho = 1$ mm. These curves make up group I. All the other curves make up group II and, for each curve, the last measurable radial distance value ρ_{last}, according to the decrease of 3 orders of magnitude relative to the reflectance value at $\rho = 1$ mm, was stored. In Fig. 3, the correlation between the last measurable radial distance value ρ_{last} and the absorption coefficient μ_a of all SRR curves of the training dataset from group II is shown. This correlation is important in the further categorization.

3.3.3 *Correlation with the reduced scattering coefficient*

A more precise observation of the fitted, logarithmic SRR curves of the training dataset showed an interesting correlation between the second derivative $R''(\rho^O) = \mathrm{d}^2\{\log[R(\rho)_{\mathrm{fit}}]\}/\mathrm{d}(\rho)^2|_{\rho=\rho^o}$ of the fitted, logarithmic SRR curve and the reduced scattering coefficient. For the second derivative, we used Eq. (4) since the derivative of a noisy SRR curve at one particular distance does not provide useable data. The second derivative, for all $\rho_{\mathrm{last}} > 4.25 \cdot (1 - 0.005)$ mm (group IIA) against the reduced scattering coefficient, is plotted in Fig. 4. The second derivative was calculated at the radial distance ρ^O where the SRR curve had a decrease of 0.7 orders of magnitude relative to the reflectance value at $\rho = 1$ mm. The

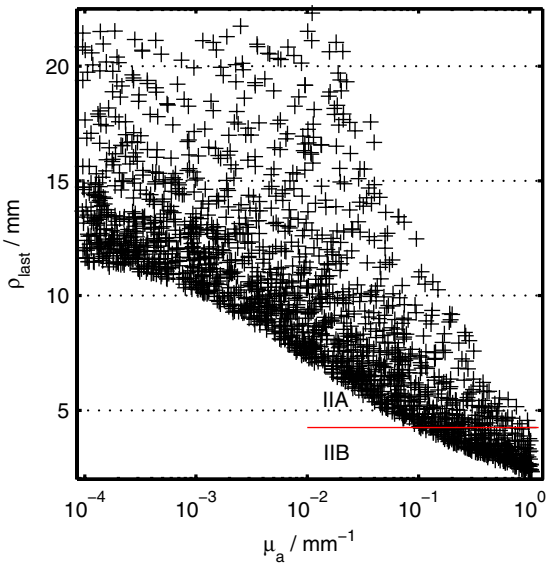

Fig. 3 Correlation between the last measurable radial distance value ρ_{last} and the absorption coefficient μ_a for all SRR curves of group II. The horizontal line represents the separation into group IIA and IIB.

value $\rho = 4.25$ mm was found empirically and some overlapping was considered. It can be seen in Fig. 4 that it is possible to categorize these SRR curves according to their reduced scattering coefficient. We have chosen 3 reduced scattering coefficient categories (IIAa, IIAb and IIAc) as shown in Fig. 4.

3.3.4 *Correlation with the absorption coefficient*

Another correlation was found between the first derivative $R'(\rho^*) = \mathrm{d}\{\log[R(\rho)_{\mathrm{fit}}]\}/\mathrm{d}(\rho)|_{\rho=\rho^*}$ of the fitted, logarithmic SRR curve and the absorption coefficient. For the same reason as above, we used Eq. (4) to calculate the derivative. The radial distance, where the SRR curve decreased 2.6 orders of magnitude relative to the reflectance value at $\rho = 1$ mm, is ρ^*. The first derivative, at a decrease of 2.6 orders of magnitude relative

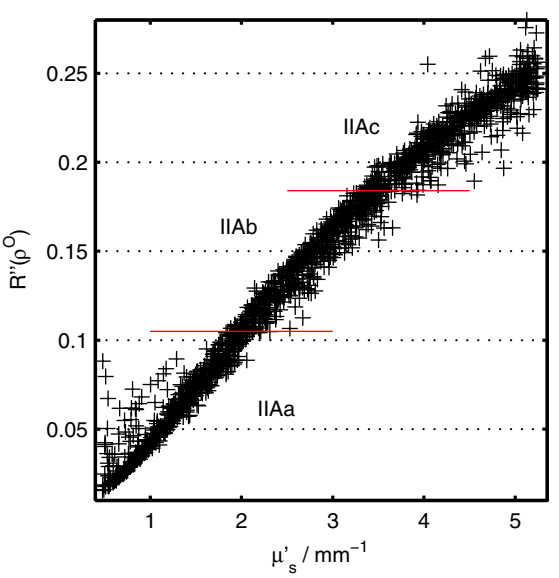

Fig. 4 Correlation between the second derivative $R''(\rho^O)$ and the reduced scattering coefficient μ_s' for all SRR curves of group IIA. The radial distance ρ^O is the position where the SRR curve decreased 0.7 orders of magnitude relative to the reflectance value at $\rho = 1$ mm.

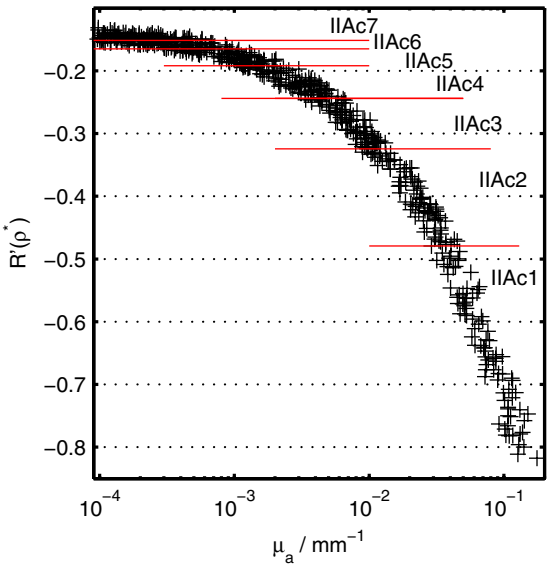

Fig. 5 Correlation between the first derivative $R'(\rho^*)$ and the absorption coefficient μ_a for all SRR curves of group IIAc. The radial distance ρ^* is the position where the SRR curve decreased 2.6 orders of magnitude relative to the reflectance value at $\rho = 1$ mm.

to the reflectance value at $\rho = 1$ mm against the absorption coefficient, is shown in Fig. 5 for all SRR curves of group IIAc. For the rest of the curves of group II, similar correlations were found.

3.3.5 *Final categorization of the SRR curves of the training dataset*

Applying the above introduced correlations, the categorization was performed and all the SRR curves of the training dataset were divided into 23 ANNs. In order to avoid problems in the edge areas, an overlapping of the ANNs was realized. Therefore, some SRR curves of the training dataset were sorted into two ANNs. In Fig. 6, the whole categorization process is summarized. All curves of group I build up the SRR curves for the training of the first ANN. Group II was first divided into another two groups, IIA and IIB, using the correlation shown in Fig. 3. Group IIA contains all SRR curves that fulfill the condition $\rho_{\text{last}} > 4.25 \cdot (1 - 0.005)$ mm and group IIB contains all SRR curves with $\rho_{\text{last}} < 4.25 \cdot (1 + 0.005)$ mm. Since all SRR curves of group IIA show a good correlation between the second derivative and the reduced scattering coefficient as plotted in Fig. 4, it is possible to sort them into further groups. For the categorization, the ranges $R''(\rho^O) < 0.105 \cdot (1 + 0.01)$ for group IIAa, $R''(\rho^O) > 0.105 \cdot (1 - 0.01)$ and $R''(\rho^O) < 0.184 \cdot (1 + 0.01)$ for group IIAb, and $R''(\rho^O) > 0.184 \cdot (1 - 0.01)$ for group IIAc

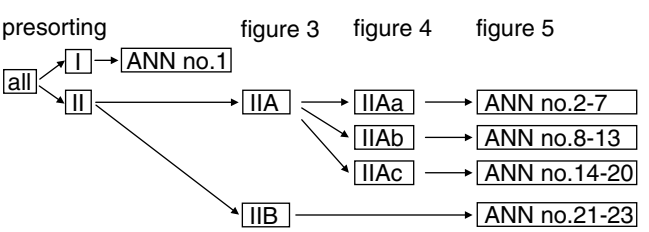

Fig. 6 Summary of the categorisation of the SRR curves into the different 23 ANNs (see ANN no. 1–23).

were considered. Therefore, group IIAa contains all SRR curves with a reduced scattering coefficient of about 0.5 mm^{-1} < μ_s' < 2 mm^{-1}, group IIAb with a reduced scattering coefficient of about 2 mm^{-1} < μ_s' < 3.5 mm^{-1}, and group IIAc with a reduced scattering coefficient of about 3.5 mm^{-1} < μ_s' < 5 mm^{-1}. In the last categorization, all curves of groups IIAa, IIAb, IIAc, and IIB were separated into different ANNs according to their correlation between the first derivative and the absorption coefficient as shown in Fig. 5. Therefore, group IIAa is divided into ANN number 2–7, group IIAb into ANN number 8–13, group IIAc into ANN number 14–20, and IIB into ANN number 21–23. The SRR curves of groups IIAa, IIAb, IIAc, and IIB were sorted according to $R'(\rho^*)$ and divided into groups of about 90 curves considering an additional overlapping of 20 curves. Finally, we obtained 23 ANNs, with between 95 and 115 SRR curves, for the training of the ANNs. In Table 1, the whole categorization process is summarized. Furthermore, the smaller optical property ranges are shown that allow a more precise training of a part of all SRR curves.

We remark that the correlations found in Figs. 4 and 5 are also valid if a solution of the diffusion theory is used for the calculation of simulated reflectance curves. As a consequence, the whole categorization process is, in general, applicable and a trained ANN can be applied for the solution of the inverse problem using other measurement geometries.

3.3.6 *Categorization of the SRR curves of the validation and testing dataset*

The 2,000 SRR curves of the validation, as well as the testing dataset, were sorted the same way as the training dataset but without overlapping. Therewith, every SRR curve is sorted precisely in one group which is evaluated by one ANN.

4 Results

4.1 *ANN*

4.1.1 *One ANN*

Applying one ANN, 10^7 iterations were performed during the training process in order to determine the weights. Thereafter, in the executing phase, a testing dataset was used consisting of 2,000 unknown SRR curves and the relative error for the absorption and reduced scattering coefficients was calculated. An average relative error of 9.5% for the absorption coefficient and 4.1% for the reduced scattering coefficient was achieved.

A fourth dataset, consisting of 123 SRR curves, was generated using MC simulations for a systematic test of the ANN. We have chosen 3 reduced scattering coefficients $\mu_s' = 1$ mm^{-1}, $\mu_s' = 2$ mm^{-1}, and $\mu_s' = 4$ mm^{-1} and 41 absorption coefficients out of the range 10^{-4} mm^{-1} < μ_a < 10^{0} mm^{-1} with equal step size in the logarithmic scale. The results for these SRR curves are shown in Fig. 7(a) for the relative error of the reduced scattering coefficient and in Fig. 7(b) for the relative error of the absorption coefficient. It can be seen that the ANN is able to determine the reduced scattering coefficient more precisely than the absorption coefficient. The relative error for the reduced scattering coefficient is higher for larger absorption coefficients [see Fig. 7(a)]. As shown in Fig. 7(b), the relative error for the absorption coefficient oscillates around the y-axis.

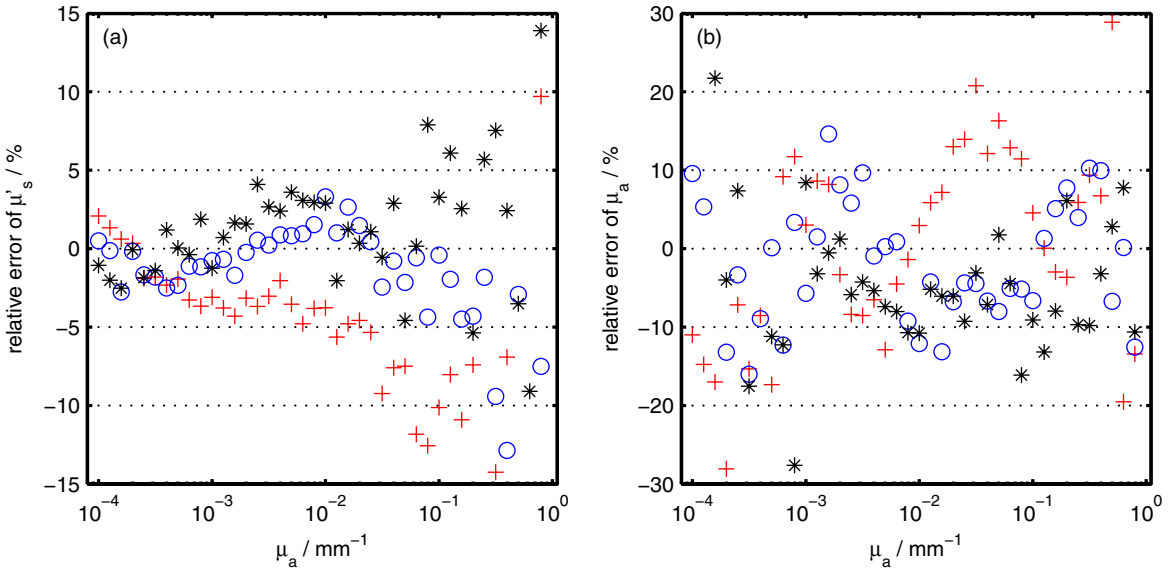

Fig. 7 Relative error of the a) reduced scattering coefficient and b) absorption coefficient is plotted against the absorption coefficient for $\mu_s' = 1$ mm^{-1} (+), $\mu_s' = 2$ mm^{-1} (O) and $\mu_s' = 4$ mm^{-1} (*). During the training process one ANN was used.

4.1.2 *Multiple ANNs*

For the training of each of the 23 ANNs, 10^5 iterations were used. Applying 100 times more iterations does not significantly improve the results for the testing dataset. During the executing phase, the same testing dataset as for one ANN was used to verify the performance of the ANNs. We calculated the average relative error for the optical properties over all 23 ANNs. An average relative error of 6.1% for the absorption coefficient and 2.9% for the reduced scattering coefficient was achieved using 10^5 iterations. Especially for the absorption coefficient, much better results were achieved using multiple ANNs for the same problem.

The results using 23 ANNs are shown in Fig. 8(a) and 8(b) for the 123 systematic SRR curves. In Fig. 8(a), it can be seen that the relative error for the reduced scattering coefficient is higher for larger absorption coefficients but overall lower as in Fig. 7(a). Figure 8(b) shows the relative error for the absorption coefficient that is obviously lower than in Fig. 7(b).

4.2 *Explanation of the Results of the ANN*

We used a solution of the DT in order to explain the errors of the ANN. Regarding the light propagation in turbid media, the DT is an often used approximation of the radiative transfer theory. We used a solution of the diffusion equation for semi-infinite media as described by Kienle and Patterson.[18]

Estimating the minimum errors to be expected for the ANN, we fit a solution of the DT to a solution of the DT with noise comparable to SRR measurements. This gives us a hint for the minimum error that can be achieved using an ANN for the solution of the inverse problem. Therefore, 123 SRR curves with 3

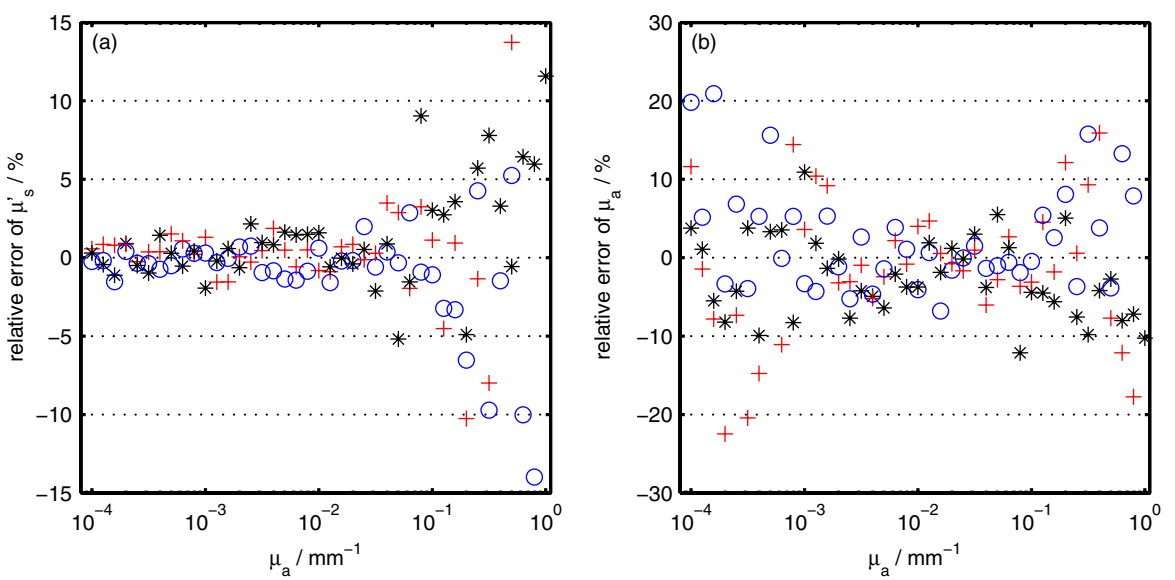

Fig. 8 Relative error of the a) reduced scattering coefficient and b) absorption coefficient is plotted against the absorption coefficient for $\mu_s' = 1$ mm^{-1} (+), $\mu_s' = 2$ mm^{-1} (O) and $\mu_s' = 4$ mm^{-1} (*). During the training process 23 ANNs were used.

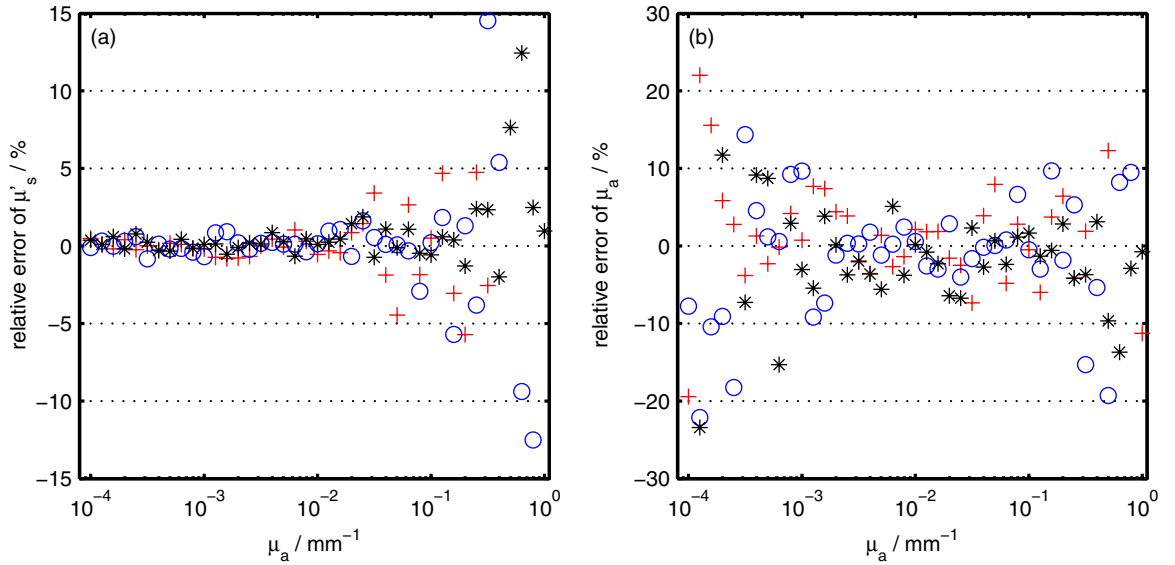

Fig. 9 Relative error of the a) reduced scattering coefficient and b) absorption coefficient is plotted against the absorption coefficient for $\mu_s' = 1$ mm^{-1} (+), $\mu_s' = 2$ mm^{-1} (O) and $\mu_s' = 4$ mm^{-1} (*). These results were achieved fitting the DT to the DT with noise.

chosen reduced scattering coefficients $\mu_s' = 1$ mm^{-1}, $\mu_s' = 2$ mm^{-1} and $\mu_s' = 4$ mm^{-1} and 41 absorption coefficients out of the range 10^{-4} mm$^{-1} < \mu_a < 10^{0}$ mm^{-1} with equal step size in the logarithmic scale were calculated with noise comparable to the MC simulations or measurement data. After the DT was fitted to the DT with noise, the relative error for the reduced scattering coefficient and absorption coefficient was determined [see Fig. 9(a) and 9(b)]. The results for the reduced scattering coefficient, shown in Fig. 9(a) have similar errors than the results of the ANNs [see Fig. 8(a)]. Also, the results for the absorption coefficient calculated with the DT [see Fig. 9(b)] and with the ANNs [see Fig. 8(b)] are comparable. The errors using the DT are marginally smaller because, using ANNs for the solution of the inverse problem, we have to take into account not only the noise of the measurements but also the error of the ANN.

4.3 *Comparison with the Results of the Diffusion Theory*

It is not possible to implement the exact setup geometry into the diffusion equation and, thus, the DT cannot be used to determine precisely the optical properties of our SRR measurements. However, an ANN can be trained with MC simulations representing the exact setup geometry and, therefore, is suitable for the determination of the optical properties of arbitrary measurement geometries (see Sec. 3.1).

If we, nevertheless, fit a solution of the diffusion equation to the simulated SRR curves, systematic errors occur. The DT was fitted to the 123 systematic SRR curves calculated with MC simulations. The relative error for μ_s' and μ_a is shown in Fig. 10(a) and 10(b), respectively. The reduced scattering coefficient is determined to be approximately 5% too low and, especially

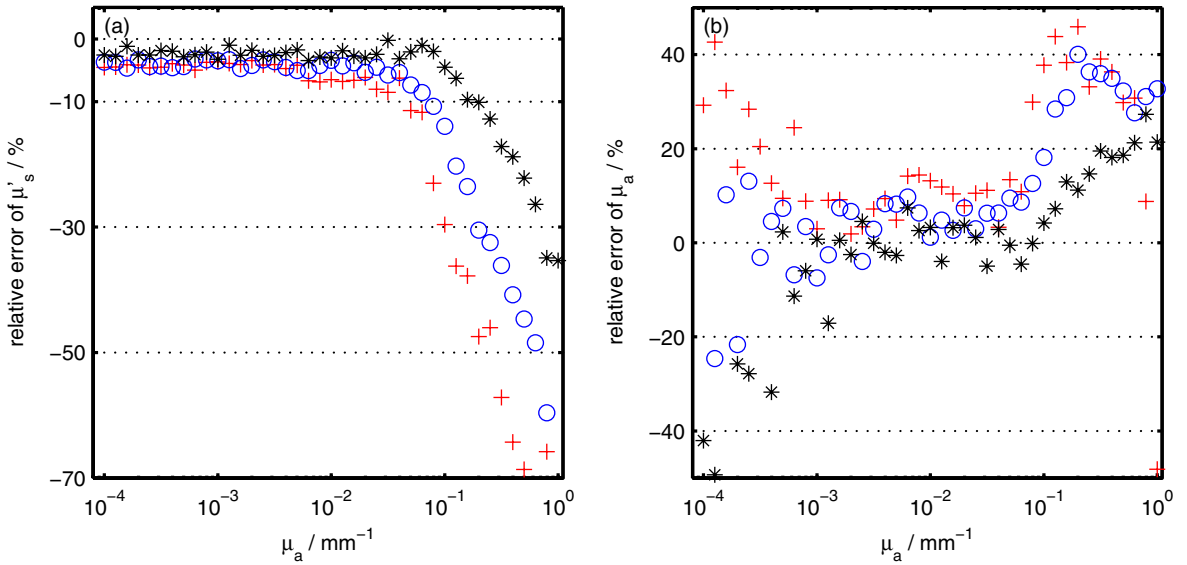

Fig. 10 Relative error of the a) reduced scattering coefficient and b) absorption coefficient is plotted against the absorption coefficient for $\mu_s' = 1$ mm^{-1} (+), $\mu_s' = 2$ mm^{-1} (O) and $\mu_s' = 4$ mm^{-1} (*). These results were achieved fitting the DT to simulated SRR curves calculated with MC simulations.

for higher μ_a, large systematic errors can be seen. In contrast, the absorption coefficient is, on average, calculated too large. Especially for smaller and higher μ_a, large relative errors occur.

5 Conclusion

For the determination of the optical properties, we used one and multiple ANNs trained with MC simulations, considering the measurement geometry. We have shown that applying more ANNs, for the determination of the optical properties of semi-infinite scattering media, improved the results significantly, especially, for the determination of the absorption coefficient. With the application of multiple ANNs for the determination of the optical properties, it is possible to determine the reduced scattering coefficient with an average relative error of 2.9% and the absorption coefficient with an average relative error of 6.1%. Whereas, one ANN leads to higher errors. The average relative error was 4.1% for the reduced scattering coefficient and the average relative error was 9.5% for the absorption coefficient.

For the performance of multiple ANNs, an important condition is the categorization of the SRR curves before the training of the ANNs. This categorization must be unique and transferable to every validation and testing SRR curve as well as to measured SRR curves. We found correlations between the first and second derivative of the SRR curve at a certain radial distance and the optical properties. For this reason, it was possible to divide different SRR curves in particular categories. A limitation of the optical property ranges into smaller categories for the absorption and reduced scattering coefficients also leads to a faster learning process of the ANN. Furthermore, we used scaled input and output values to improve the performance of the ANN. After the input and output values for the testing dataset were prepared, it took 734 ms to determine the optical properties of 2,000 SRR curves, therewith, about 0.37 ms per SRR curve using a single processor of a state of the art computer.

Using the DT, a theoretical curve was fitted to a theoretical curve with noise and the results were compared with the results of the multiple ANNs. This comparison showed similar errors for the optical properties as shown in Figs. 8(a), 8(b), 9(a), and 9(b). Thus, using the multiple ANNs, we almost reached the same errors as using the DT that was fitted to the DT with noise, i.e., the performance of the multiple ANNs is close to the theoretical optimum. We remark that the multiple ANNs were trained with MC simulations considering the measurement geometry of our measurement setup and, therefore, can be used to determine the optical properties of measured SRR curves. We would like to point out that the determination of the optical properties from measured reflectance data is also possible using other particular measurement systems since the correlations found in Figs. 4 and 5 are also valid if a solution of the diffusion theory is used for the calculation of simulated reflectance curves. Therefore, the ANNs have to be trained with simulated measurement curves considering the actual measurement geometry.

In addition, we determined the optical properties, using the DT, that was fitted to the simulated SRR curves calculated with MC simulations. The results for the optical properties show large systematic errors. As a consequence, the DT cannot be used to determine precisely the optical properties from measurement data where the setup geometry has to be taken into account.

Acknowledgments

M. Jäger was financially supported by a post gradual Ph.D. scholarship granted by Ulm University.

References

1. L. H. Wang, X. M. Zhao, and S. L. Jacques, "Computation of the optical properties of tissues from light reflectance using a neural network," *Proc. SPIE* **2134A**, 391–399 (1994).
2. J. T. Bruulsema et al., "Correlation between blood glucose concentration in diabetics and noninvasively measured tissue optical scattering coefficient," *Opt. Lett.* **22**(3), 190–192 (1997).
3. F. Bevilacqua et al., "In vivo local determination of tissue optical properties: applications to human brain," *Appl. Opt.* **38**(22), 4939–4950 (1999).
4. T. J. Pfefer et al., "Reflectance-based determination of optical properties in highly attenuating tissue," *J. Biomed. Opt.* **8**(2), 206–215 (2003).
5. J. Choi et al., "Noninvasive determination of the optical properties of adult brain: near-infrared spectroscopy approach," *J. Biomed. Opt.* **9**(1), 221–229 (2004).
6. D. Sharma et al., "Evaluation of a fiberoptic-based system for measurement of optical properties in highly attenuating turbid media," *Biomed. Eng. Online* **5**, 49 (2006).
7. D. Comelli et al., "In vivo time-resolved reflectance spectroscopy of the human forehead," *Appl. Opt.* **46**(10), 1717–1725 (2007).
8. T. J. Farrell, B. C. Wilson, and M. S. Patterson, "The use of a neural network to determine tissue optical properties from spatially resolved diffuse reflectance measurements," *Phys. Med. Biol.* **37**(12), 2281–2286 (1992).
9. T. J. Farrell et al., "A CCD and neural network based instrument for the non-invasive determination of tissue optical properties in-vivo," *Proc. SPIE* **2135**, 117–128 (1994).
10. A. Kienle et al., "Spatially resolved absolute diffuse reflectance measurements for noninvasive determination of the optical scattering and absorption coefficients of biological tissue," *Appl. Opt.* **35**(13), 2304–2314 (1996).
11. D. Warncke et al., "A neural network based approach for determination of optical scattering and absorption coefficients of biological tissue," *J. Phys. Conf. Ser.* **178**(1), 012047 (2009).
12. L. Zhang, Z. Wang, and M. Zhou, "Determination of the optical coefficients of biological tissue by neural network," *J. Mod. Opt.* **57**(13), 1163–1170 (2010).
13. Q. Wang, K. Shastri, and T. J. Pfefer, "Experimental and theoretical evaluation of a fiber-optic approach for optical property measurement in layered epithelial tissue," *Appl. Opt.* **49**(28), 5309–5320 (2010).
14. Q. Wang et al., "Broadband ultraviolet-visible optical property measurement in layered turbid media," *Biomed. Opt. Express* **3**(6), 1226–1240 (2012).
15. C. Yaqin et al., "Determination of tissue optical properties from spatially resolved relative diffuse reflectance by PCA-NN," in *Proc. Int. Conf. on Neural Networks and Signal Process.*, Vol. 1, pp. 369–372, IEEE, Nanjing (2003).
16. M. Jäger and A. Kienle, "Non-invasive determination of the absorption coefficient of the brain from time-resolved reflectance using a neural network," *Phys. Med. Biol.* **56**(11), N139–N144 (2011).
17. M. Jäger and A. Kienle, "Non-invasive determination of the optical properties of the human head using a neural network," *Proc. SPIE* **8088**, 80880H (2011).
18. A. Kienle and M. S. Patterson, "Improved solutions of the steady-state and the time-resolved diffusion equations for reflectance from a semi-infinite turbid medium," *J. Opt. Soc. Am. A* **14**(1), 246–254 (1997).
19. A. Liemert and A. Kienle, "Light transport in three-dimensional semi-infinite scattering media," *J. Opt. Soc. Am. A* **29**(7), 1475–1481 (2012).
20. L. Wang, S. L. Jacques, and L. Zheng, "MCML-Monte Carlo modeling of light transport in multi-layered tissues," *Comput. Meth. Prog. Bio.* **47**(2), 131–146 (1995).
21. F. Foschum, M. Jäger, and A. Kienle, "Fully automated spatially resolved reflectance spectrometer for the determination of the absorption and scattering in turbid media," *Rev. Sci. Instrum.* **82**(10), 103104 (2011).
22. R. Michels, F. Foschum, and A. Kienle, "Optical properties of fat emulsions," *Opt. Express* **16**(8), 5907–5925 (2008).
23. A. Kienle and F. Foschum, "250 years Lambert surface: does it really exist?," *Opt. Express* **19**(5), 3881–3889 (2011).
24. L. R. Poole, D. D. Venable, and J. W. Campbell, "Semianalytic Monte Carlo radiative transfer model for oceanographic lidar systems," *Appl. Opt.* **20**(20), 3653–3656 (1981).
25. J. M. Boone, V. G. Sigillito, and G. S. Shaber, "Neural networks in radiology: an introduction and evaluation in a signal detection task," *Med. Phys.* **17**(2), 234–241 (1990).